BIOCHEMISTRY
including biophysical chemistry & molecular biology

Article

pubs.acs.org/biochemistry

Structural Basis for Assembly of the Mn^{IV}/Fe^{III} Cofactor in the Class Ic Ribonucleotide Reductase from *Chlamydia trachomatis*

Laura M. K. Dassama,[†,§] Carsten Krebs,[†] J. Martin Bollinger, Jr.,[†] Amy C. Rosenzweig,[‡] and Amie K. Boal*[,‡,∥]

[†]Department of Chemistry and Department of Biochemistry and Molecular Biology, The Pennsylvania State University, University Park, Pennsylvania 16802, United States

[‡]Department of Molecular Biosciences and Department of Chemistry, Northwestern University, Evanston, Illinois 60208, United States

Supporting Information

ABSTRACT: The class Ic ribonucleotide reductase (RNR) from *Chlamydia trachomatis* (*Ct*) employs a Mn^{IV}/Fe^{III} cofactor in each monomer of its β_2 subunit to initiate nucleotide reduction. The cofactor forms by reaction of Mn^{II}/Fe^{II}-β_2 with O_2. Previously, *in vitro* cofactor assembly from apo β_2 and divalent metal ions produced a mixture of two forms, with Mn at site 1 (Mn^{IV}/Fe^{III}) or site 2 (Fe^{III}/Mn^{IV}), of which the more active Mn^{IV}/Fe^{III} product predominates. Here we have addressed the basis for metal site selectivity by determining X-ray crystal structures of apo, Mn^{II}, and Mn^{II}/Fe^{II} complexes of *Ct* β_2. A structure obtained anaerobically with equimolar Mn^{II}, Fe^{II}, and apoprotein reveals exclusive incorporation of Mn^{II} at site 1 and Fe^{II} at site 2, in contrast to the more modest site selectivity achieved previously. Site specificity is controlled thermodynamically by the apoprotein structure, as only minor adjustments of ligands occur upon metal binding. Additional structures imply that, by itself, Mn^{II} binds in either site. Together, the structures are consistent with a model for *in vitro* cofactor assembly in which Fe^{II} specificity for site 2 drives assembly of the appropriately configured heterobimetallic center, provided that Fe^{II} is substoichiometric. This model suggests that use of a Mn^{IV}/Fe^{III} cofactor *in vivo* could be an adaptation to Fe^{II} limitation. A 1.8 Å resolution model of the Mn^{II}/Fe^{II}-β_2 complex reveals additional structural determinants for activation of the cofactor, including a proposed site for side-on (η^2) addition of O_2 to Fe^{II} and a short (3.2 Å) Mn^{II}–Fe^{II} interionic distance, promoting formation of the Mn^{IV}/Fe^{IV} activation intermediate.

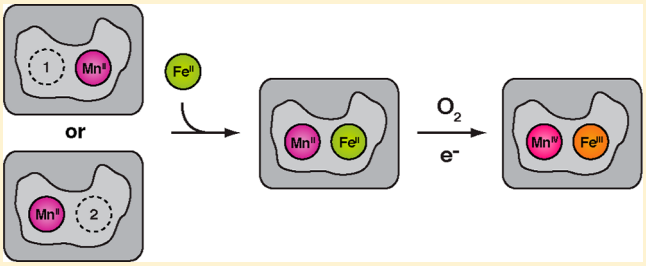

Ribonucleotide reductases (RNRs) catalyze the conversion of ribonucleotides to 2′-deoxyribonucleotides, initiating the only known pathway for nucleotide production in the *de novo* synthesis and repair of DNA.[1,2] Class I RNRs, such as the enzymes from all mammals and many aerobic bacteria and viruses, initiate nucleotide reduction with a metallocofactor, assembled and stored in each monomer of the homodimeric β_2 subunit. The metallocofactor in β_2 transiently oxidizes a Cys residue ~35 Å away in a monomer of the homodimeric α_2 subunit via a reversible long-range radical-translocation (RT) process.[3] The resultant Cys radical abstracts a hydrogen atom from the 3′-carbon of the substrate in the first step of the transformation that reduces the 2′-carbon.[4,5]

The use of different metallocofactors by the RNRs in class I is the basis for their further division into subclasses a–c. Members of class Ia and class Ib employ carboxylate-bridged homodinuclear $Fe_2^{III/III}$ and $Mn_2^{III/III}$ clusters, respectively (Figure 1A–E), in conjunction with adjacent tyrosyl radicals ($Tyr^{\bullet}$s) to generate their Cys radicals.[3,6−10] The orthologs from aerobically growing *Escherichia coli* (*Ec*, Ia) and *Bacillus subtilis* (*Bs*, Ib) are the most extensively studied versions of these enzymes. The homodinuclear cofactors can be formed by addition of the divalent metals to metal-free (apo) protein and reaction of the reduced metal centers with an oxidant: O_2 in the class Ia orthologs[2,3] and $O_2^{\bullet-}$ (generated from O_2 by a flavoprotein activase) in the class Ib orthologs.[9] In each case, reaction with the oxidant produces a high-valent[9,11] intermediate that oxidizes the essential Tyr residue to yield the active metallocofactor. The only biochemically characterized representative of class Ic, the ortholog from the human pathogen *Chlamydia trachomatis* (*Ct*), has a Phe residue at the position corresponding to the $Tyr^{\bullet}$ in the class Ia and Ib orthologs. *In vitro*, the *Ct* β_2 protein has been shown to assemble a heterodinuclear Mn^{IV}/Fe^{III} cofactor in each β monomer and to use this cofactor in catalysis.[12−15] The Mn^{IV} ion functionally replaces the $Tyr^{\bullet}$ employed by the Ia and Ib orthologs. Analysis of available genome sequences suggests that many more (>100) class Ic orthologs exist,[16] but the ability of these additional (putative) RNRs to function with Mn^{IV}/Fe^{III}

Received: June 24, 2013
Revised: August 6, 2013
Published: August 7, 2013

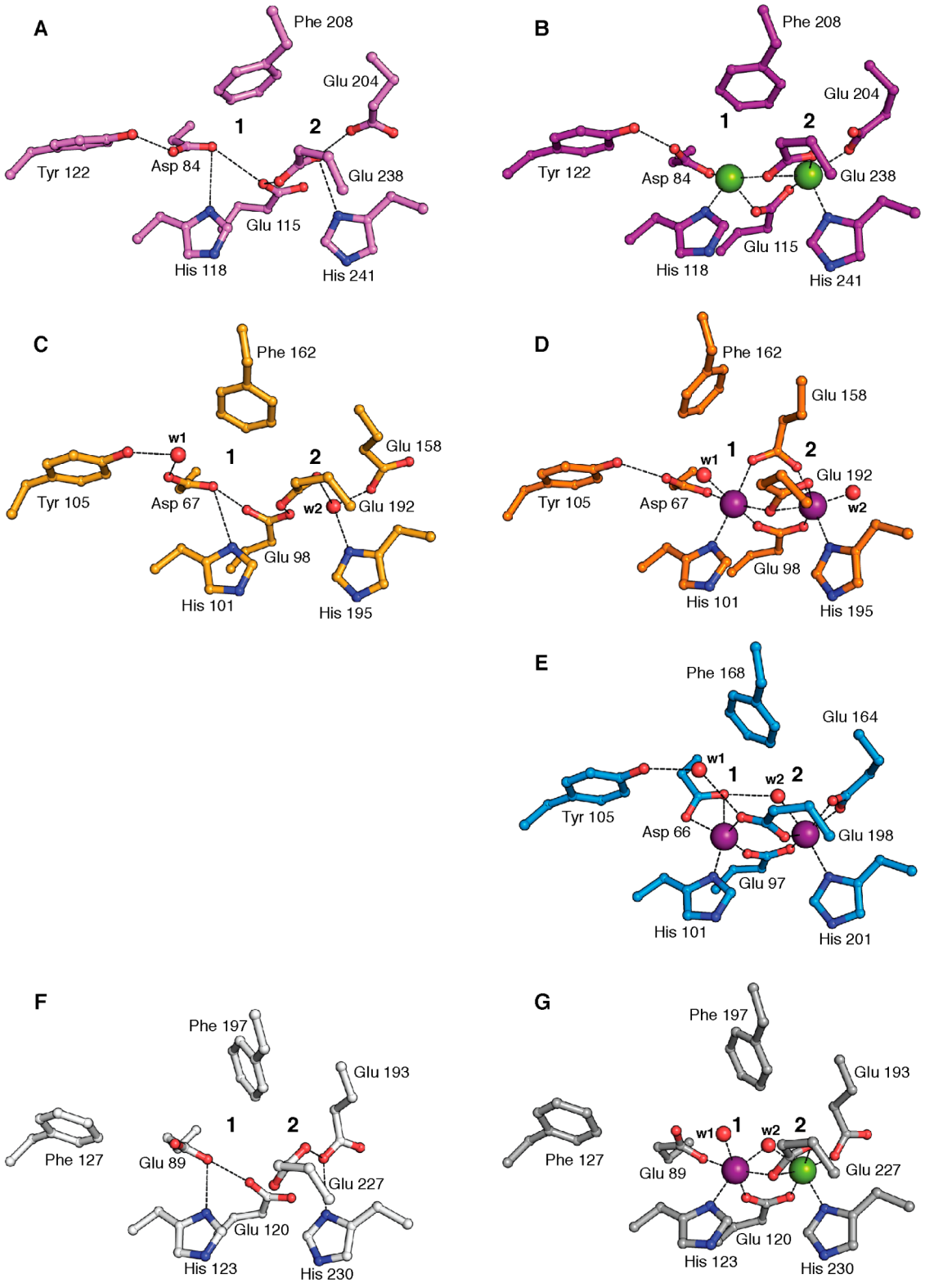

Figure 1. Comparison of the apo and reduced metallocofactor sites in class I β_2 proteins: (A) *Ec* class Ia apo β_2,[23] (B) *Ec* class Ia $Fe_2^{II/II}$-β_2 (PDB entry 1PIY), (C) *Ec* class Ib apo β_2 (PDB entry 4M1F), (D) *Ec* class Ib $Mn_2^{II/II}$-β_2 (PDB entry 3N37), (E) *Bs* class Ib $Mn_2^{II/II}$-β_2 (PDB entry 4DR0), (F) *Ct* class Ic apo β_2, and (G) *Ct* class Ic Mn^{II}/Fe^{II}-β_2. Ligands and selected outer sphere residues are shown as sticks. Mn^{II} and Fe^{II} ions are shown as purple and green spheres, respectively. Ordered water molecules are shown as red spheres. Metal–ligand interactions and selected hydrogen bonds are shown as gray dashed lines.

cofactors has not been established. Moreover, *in vivo* usage of such a cofactor by any class Ic RNR remains to be demonstrated.

Since its discovery, the structure of the novel heterodinuclear cofactor of *Ct* RNR and its mechanism of assembly have been extensively studied.[12,13,15,17−20] It was shown that

dx.doi.org/10.1021/bi400819x | *Biochemistry* 2013, 52, 6424−6436

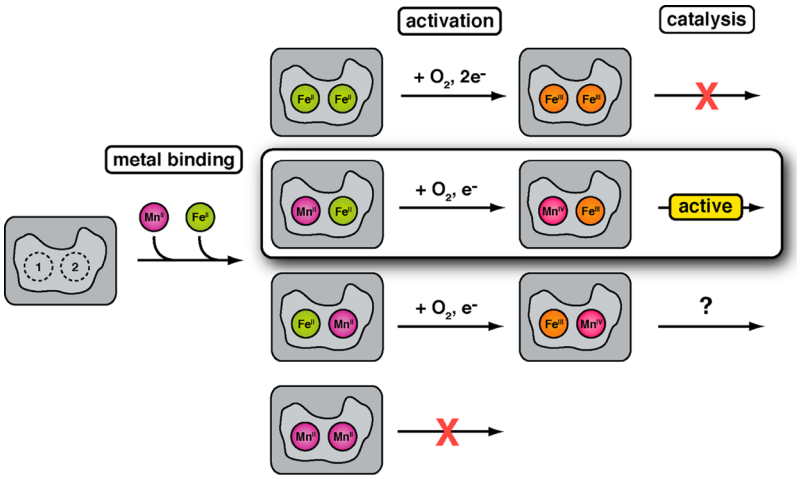

Figure 2. Schematic depiction of productive and unproductive steps during the *in vitro* assembly of the Mn/Fe metallocofactor in *Ct* β_2. In the metal binding step, four possible cluster types can be assembled. $Mn_2^{II/II}$ clusters do not react with O_2. $Fe_2^{II/II}$ clusters react with O_2 to form $Fe_2^{III/III}$ clusters that are inactive in nucleotide reduction. Mn^{II}/Fe^{II} and Fe^{II}/Mn^{II} clusters can both react with O_2, and it is possible that each may be competent to initiate nucleotide reduction. However, the data presented here and previously[21] suggest the Mn^{II}/Fe^{II} form is the relevant precursor to the active cofactor.

apo β_2 can assemble the active cofactor from the divalent metals and O_2 via a Mn^{IV}/Fe^{IV} intermediate.[13] An electron shuttled to the cluster (via neighboring Tyr 222 and Trp 51) reduces the Fe^{IV} site of the intermediate to form the stable and active Mn^{IV}/Fe^{III} state.[14] Two separate X-ray crystallographic studies showed that forms of β_2 having Mn at site 1 (this cofactor form is hereafter denoted Mn^{IV}/Fe^{III}) predominate upon assembly of the cofactor either *in vitro*[21] or during heterologous expression in *E. coli*.[22] Additionally, the former study revealed some Mn occupancy in site 2 under certain metal loading conditions, suggesting production of smaller amounts of the Fe^{III}/Mn^{IV} complex.[21] A negative correlation between the prevalence of this complex in different preparations and their catalytic activities implied that the form of the protein with Mn at site 2 is less active or inactive (Figure 2).

The steps of the cofactor assembly reaction preceding the Mn^{IV}/Fe^{IV} intermediate remain poorly understood. For example, almost nothing is known about how the two different divalent metal ions selectively occupy their functional sites, nor is the mode of addition of O_2 to the Mn^{II}/Fe^{II} (or Fe^{II}/Mn^{II}) state known. In previous work, two different reconstitution procedures yielded different distributions of the more active Mn^{IV}/Fe^{III} and less active (or inactive) Fe^{III}/Mn^{IV} forms.[21] In the first procedure (procedure 1), apo β_2 was preloaded with 1.5 equiv of Mn^{II} per β monomer (slightly greater than the experimentally determined stoichiometry of functional sites) in the presence of ambient O_2, and Fe^{II} was then added very slowly to a final level of 0.75 equiv per monomer. The underlying rationale was to use the anticipated lability of Mn^{II} in the site designed to bind Fe^{II} to direct incorporation of Fe^{II} into this site, with rapid addition of O_2 irreversibly trapping a single cluster form. This procedure yielded Mn occupancy primarily of site 1 but with significant additional occupancy of site 2. In the second procedure (procedure 2), the quantity of Mn^{II} initially added was diminished to less than the experimental stoichiometry of functional sites and varied systematically. Fe^{II} was then injected rapidly in the presence of ambient O_2. Procedure 2 resulted in diminished Mn occupancy of site 2 and greater catalytic activity on a per Mn basis. However, catalytically inactive $Fe_2^{III/III}$ clusters predominated at the lowest initial Mn^{II}/β ratios. Permitting the Mn/Fe cofactor to assemble during overexpression of *Ct* β_2 in *E. coli* with Mn^{II} supplementation resulted in an outcome similar to that of *in vitro* assembly procedure 2.[22] The propensity of the *Ct* β_2 protein to assemble multiple cluster forms in addition to the (more) active configuration motivated further exploration of the structural and dynamic bases for the selective assembly of the most active state.

For the class Ia and Ib RNRs, comparison of the X-ray crystal structures of the apo β_2 proteins,[23,24] their $Mn_2^{II/II}$ and/or $Fe_2^{II/II}$ complexes,[25−29] and the corresponding oxidized states[7,8,28,30] revealed the structural adjustments that accompany metallocofactor assembly and activation. Expanding the comparison to include published structures of oxidized *Ct* β_2 shows that, although orthologs of each subclass are distinguished from the members of the other two by the combination of metal ions utilized in the active cofactor, the structures of the oxidized metallocofactors remain remarkably similar across all three subclasses.[2] In each case, the site comprises two His and four carboxylate (Glu or Asp) ligands arranged similarly around the metal subsites. This structural similarity has been cited as a rationale for improper incorporation of Mn^{II} into class Ia β_2 proteins and Fe^{II} into class Ib and Ic β_2 proteins.[31] Nevertheless, analysis of the class Ia $Fe_2^{II/II}$-β_2 and class Ib $Mn_2^{II/II}$-β_2 structures shows that the surrounding protein scaffold provides distinct coordination environments for Mn^{II} or Fe^{II} (Figure 1A−E), channels tailored to transport a specific oxidant (O_2 or $O_2^{\bullet-}$) to the metal binding site, and, in the class Ib system, a distinct interaction surface for binding of an accessory protein.[25−27]

In this work, we investigate whether the class Ic *Ct* β_2 subunit might possess specific adaptations (to its metal sites or the surrounding protein) first to promote assembly of the proper (Mn^{II}/Fe^{II}) reduced precursor to the functional cofactor and then to direct its reaction with O_2 to generate the active Mn^{IV}/Fe^{III} state. Structures of the apo and Mn^{II}/Fe^{II} complexes were determined by X-ray crystallography; the latter complex was prepared by cocrystallization of β_2 in the presence of stoichiometric Mn^{II} and Fe^{II} under anoxic conditions. These structures show that the Mn^{II}/Fe^{II} state (with Mn at site 1, as

dx.doi.org/10.1021/bi400819x | *Biochemistry* 2013, 52, 6424−6436

previously concluded)[21,22] assembles efficiently with only low levels of incorrect cluster configurations (Fe^{II}/Mn^{II}, $Mn_2^{II/II}$, or $Fe_2^{II/II}$) (Figure 2). The structures thus imply that the metal binding site has sufficient inherent selectivity to direct Mn^{II} to site 1 and Fe^{II} to site 2 as long as the metals are provided in the proper stoichiometry and metal incorporation is controlled by thermodynamics (i.e., by allowing sufficient time for equilibration of the metals with the protein prior to addition of O_2) rather than kinetics. Indeed, preparations reconstituted in this manner were found by electron paramagnetic resonance (EPR) spectroscopic analysis to be more homogeneous than those produced in the previous studies and by activity assays to be the most active preparations characterized to date. Intriguingly, diffraction data on crystals prepared from solutions of apoprotein supplemented with Mn^{II} only reveal Mn occupancy of both metal sites, although not necessarily simultaneously, even with substoichiometric quantities of Mn^{II}, suggesting that the selective assembly of the Mn^{II}/Fe^{II} reactant state might arise from the preference of Fe^{II} for site 2. Neither the surprisingly high degree of site selectivity in metal binding nor the efficient reaction of the resultant Mn^{II}/Fe^{II} complex with O_2 appears to be coupled to protein dynamics, as the dispositions of the metal ligands in the apo and Mn^{II}/Fe^{II} metalated forms are virtually identical, and only minor adjustments (displacement of a water and rearrangement of a single carboxylate residue) are seen upon oxidation of the cluster. Comparison of the structures of the reduced and oxidized forms suggests that Fe^{II} is poised to add O_2 in a side-on fashion during activation of the cofactor, leading to subsequent coupling to the Mn ion concomitant with cleavage of the O−O bond.

EXPERIMENTAL PROCEDURES

Overexpression and Purification of Apo *Ct* β_2. The construction of the plasmid containing the gene (*nrdB*) that encodes *Ct* β_2 has been described previously.[12] This construct expresses the protein with an N-terminal His_6 affinity tag comprising 20 total additional residues. Procedures for purification of the protein in its apo form have been described previously.[12]

General Crystallographic Methods. All crystallographic data sets were collected at the Life Sciences Collaborative Access Team (LS-CAT) and the General Medical Sciences and National Cancer Institutes Structural Biology Facility (GM/CA-CAT) beamlines at the Advanced Photon Source (Argonne National Laboratory, Argonne, IL). Data sets were indexed, integrated, and scaled with the HKL2000 software package.[32] All structures were determined by molecular replacement using PHASER[33] with the structure of an $Fe_2^{III/III}$-β monomer (PDB entry 1SYY) as the search model. The resulting initial models were used as the basis for further refinement and model building with Refmac5[34] and Coot,[35] respectively. Tables S1−S8 of the Supporting Information report all data collection and refinement statistics. Figures were generated with the PyMOL Molecular Graphics System.[36] Structural superpositions were performed using the secondary-structure matching (SSM) alignment method.[37] Electron density maps were calculated with FFT.[38] Fe-specific maps were generated using a subtraction procedure[39] with FFT and SFTOOLS.

Determination of the X-ray Crystal Structure of Apo β_2. Crystals of apo β_2 were grown from solutions of 10−30 mg/mL protein in 20 mM HEPES (pH 7.6) and 5−10% glycerol using the hanging drop vapor diffusion method at room temperature with 100 mM HEPES (pH 7.5), 200 mM sodium acetate, and 10% (w/v) PEG 3000 as the precipitant. Colorless crystals appeared within 2 weeks and were overlaid with a cryoprotectant solution [well solution supplemented with 50% (v/v) glycerol], mounted on rayon loops, and flash-frozen in liquid nitrogen for data collection. Data collection and refinement statistics are reported in Table S1 of the Supporting Information.

The asymmetric unit (ASU) consists of four β monomers arranged into two β_2 dimers. As observed previously,[21] the N-terminal affinity tag mediates an intermolecular interaction between adjacent β_2 dimers in three of the four molecules in the ASU. The final model includes residues 1−322 for chain A (with nine additional residues from the affinity tag), residues 1−328 for chain B (with eight additional tag residues), residues 1−329 for chain C (with two additional tag residues), residues 1−328 for chain D (with six additional tag residues), and 888 water molecules. Ramachandran plots generated with Molprobity[40] indicate that 99.5% of the residues are in favorable regions and 100% of the residues in the allowed and generously allowed regions.

Determination of the X-ray Crystal Structure of Mn^{II}/Fe^{II}-β_2. Apo β_2 was loaded with 1 equiv (per β monomer) of $MnCl_2$ [10 mM solution in 50 mM HEPES (pH 7.5)] and degassed via five cycles of vacuum purge followed by refilling with Ar on a Schlenk line. All subsequent manipulations were conducted with stringently degassed solutions of crystallization and cryoprotection reagents in a Coy anaerobic chamber with a 5% H_2/95% N_2 atmosphere. One equivalent (per β monomer) of $(NH_4)_2Fe(SO_4)_2$ [10 mM solution in 50 mM HEPES (pH 7.5)] was added to the degassed protein solution. Crystals of the metal-loaded protein were grown by hanging drop vapor diffusion at room temperature with 100 mM HEPES (pH 7.2), 200 mM sodium acetate, and 10% (w/v) PEG 3000 as the precipitant. Colorless or very light green crystals appeared within 2 weeks. We prepared crystals for data collection by covering the crystal drop with a cryoprotectant solution [well solution supplemented with 50% (v/v) PEG 400], mounting the crystal on rayon loops, and flash-freezing the crystal in liquid nitrogen. Data collection and refinement statistics are reported in Table S2 of the Supporting Information.

The asymmetric unit (ASU) consists of four β monomers with the same arrangement described above for crystals of apo β_2. The final model includes residues 1−327 for chain A (with six additional residues from the affinity tag), residues 1−320 for chain B (with nine additional tag residues), residues 1−327 for chain C (with six additional tag residues), residues 1−328 for chain D (with two additional tag residues), four Mn^{II} ions, four Fe^{II} ions, one acetate molecule, one PEG 400 molecule, and 1027 water molecules. Ramachandran plots generated with Molprobity[40] show that 99.4% of the residues are in favorable regions and 100% of the residues in the allowed and generously allowed regions. Metal ion occupancies were independently refined with PHENIX.[41] Table 1 and Table S9 of the Supporting Information show anomalous map peak heights for each metal binding site.

Tables S3, S4, S7, and S8 of the Supporting Information present crystallization conditions and data collection statistics for crystals of the protein grown with Mn^{II} only (at 1 or 2 equiv per β Fe^{II} only or 1 equiv of each metal). Mn^{II}-only samples were crystallized outside of the anaerobic chamber as described for the apoprotein. Fe^{II}-containing samples were loaded with metal and then crystallized in the anaerobic chamber, as

dx.doi.org/10.1021/bi400819x | *Biochemistry* 2013, 52, 6424−6436

Table 1. Anomalous Peak Heights (σ) at the Mn Absorption Edge for *Ct* β_2 Crystallographic Data Sets

crystal	chain	site 1	site 2
Mn^{II}/Fe^{II}-β_2	A	18.3	4.0
	B	14.9	4.1
	C	14.7	5.0
	D	14.7	2.1
Mn^{IV}/Fe^{III}-β_2	A	13.1	2.4
procedure 3A	B	8.6	3.7
	C	11.5	3.5
	D	5.6	2.4
Mn^{IV}/Fe^{III}-β_2	A	6.3	–
procedure 3B	B	7.6	–
	C	5.3	1.4
	D	4.0	–

described for the Mn^{II}/Fe^{II}-β_2 crystals. These samples were later exposed to O_2 during crystallization or crystal harvest.

Preparation of Mn^{IV}/Fe^{III}-β_2 for Activity Measurements. As summarized in Table 2, different ratios of Mn^{II} and Fe^{II} were premixed in an anoxic chamber and added to an O_2-free solution of apo β_2. After a brief incubation (5−10 min), a solution of O_2-saturated (at 5 °C) reaction buffer [100 mM HEPES and 10% (v/v) glycerol (pH 7.6) at 4 °C] was added to the Mn^{II}/Fe^{II}-β_2 solution. Excess and/or weakly bound metals were removed as previously described.[20,21] The quantity of each metal retained was determined by inductively coupled plasma atomic emission spectroscopy (ICP-AES).

Crystallization of Mn^{IV}/Fe^{III}-β_2. Crystals of the Mn^{IV}/Fe^{III} form of β_2 were obtained from 10−30 mg/mL protein solutions prepared in 20 mM HEPES (pH 7.6) and 5−10% glycerol. The Mn^{IV}/Fe^{III} form was generated from the apoprotein by the reconstitution procedure described above, and crystals were grown using the hanging drop vapor diffusion method at room temperature with either 100 mM HEPES (pH 7.0), 200 mM sodium acetate, and 5% (w/v) PEG 3000 or 100 mM HEPES (pH 7.2), 200 mM sodium acetate, and 5% (w/v) PEG 3000 as the precipitant. Pale yellow crystals appeared within 2 weeks and were overlaid with a cryoprotectant solution [precipitant solution supplemented with 50% (v/v) PEG 400], mounted on rayon loops, and flash-frozen in liquid nitrogen for data collection. Data collection statistics are provided in Tables S5 and S6 of the Supporting Information.

Table 2. Metal Incorporation (equivalents per β) and Enzymatic Activity Analysis for Mn^{IV}/Fe^{III}-β_2

preparation	Mn^{II} added	Fe^{II} added	Mn retained	Fe retained	ν/β (s^{-1})	ν/Mn (s^{-1})
procedure 3A	2.0	0.65	0.40	0.42	0.50	1.16
procedure 3B	1.0	1.0	0.48	0.68	0.56	1.25
procedure 3C	0.65	2.0	0.38	1.26	0.48	1.24
procedure 1[a]	1.50	0.75	0.55	0.65	0.38	0.70
procedure 2[a]	0.15	1.0	0.13	0.73	0.16	1.10

[a]As reported in ref 21.

RESULTS

X-ray Crystal Structure of Apo β_2. The crystal structure of apo β_2 (Table S1 of the Supporting Information) was determined to a resolution of 1.7 Å and contains four β monomers arranged into two β_2 dimers. Together, these afford four independent views of the metal binding site prior to initiation of metallocofactor assembly. The apoprotein adopts an overall fold that is nearly identical to that in metal-loaded forms of the protein (Figure S1 of the Supporting Information) (0.46 Å root-mean-square deviation for 317 Cα atoms in a single β monomer). Electron density maps of the site (Figure S2 of the Supporting Information) show that the ligands are generally well-ordered despite the absence of metal ions. Anomalous scattering data sets collected at the Mn and Fe X-ray absorption K-edges (Table S1 of the Supporting Information) yielded difference maps confirming the absence of these metal ions from the cofactor site and elsewhere in the structure (Figure S2 of the Supporting Information). Additionally, significant electron density for ordered solvent is not observed at the cofactor site, although in some views, weak positive difference density that could potentially arise from disordered water molecules was observed.

The metal-coordinating residues (Figure 1F) cluster together within hydrogen bonding distance of one another. Such close clustering of ligands indicates protonation of some of the Asp/Glu/His metal-binding residues, as proposed for the class Ia and Ib apo β_2 proteins.[23,24] In the structure of the *Ct* class Ic apo β_2 protein, the metal binding residues near metal site 2 (Glu 227, Glu 193, and His 230) associate particularly tightly (Figure 1F), further highlighting that some of them are protonated (Figure S3 of the Supporting Information). Near site 1, *Ct* β_2 differs from the class Ia and Ib proteins in its substitution of a Glu for an Asp in the coordination sphere and a Phe for a Tyr in the second sphere at position 127 (*Ct* β_2 numbering).[42] In the class Ia and Ib apo β_2 structures,[23,24] the shorter Asp side chain and Tyr residue in the second sphere interact with each other and result in a more open configuration at site 1. In class Ic β_2, the larger Glu side chain at position 89 allows the residue to hydrogen bond with both the other site 1 ligand His 123 and the bridging residue Glu 120. This interaction suggests that both His 123 and Glu 120 might be protonated (Figure S3 of the Supporting Information). The Tyr to Phe substitution removes a competing hydrogen bond in the second sphere, permitting Glu 120 to engage in closer and more numerous interactions with the other site 1 ligands. The Phe 127 substitution, in combination with the position of surrounding hydrophobic residues (Figure S4 of the Supporting Information), further encourages close packing of the ligands near site 1.

Whereas the ligands associated with each individual site interact strongly with one another in the apoprotein, very little hydrogen bonding is observed between sites (Figure S3 of the Supporting Information). Only one potential interaction is possible, between Glu 120 and Glu 193. However, the orientation is suboptimal, and the hydrogen bonding capacity of Glu 193 is fully saturated by its interactions with Glu 227 and His 230. The position of hydrophobic residue Phe 197 further defines a steric barrier between sites (Figure S4 of the Supporting Information). Interestingly, the orientation of this residue does not change upon metal loading (*vide infra*), in contrast to what is observed in other class I β_2 structures (Figure 1A−D). The lack of hydrogen bonds and the presence of a steric barrier between the sites may limit cooperative metal binding in this system to aid in assembly of a heterobimetallic center.

X-ray Crystal Structure of Mn^{II}/Fe^{II}-β_2. An X-ray crystal structure of the reduced Mn^{II}/Fe^{II} form of the protein was determined to a resolution of 1.80 Å and obtained by loading

dx.doi.org/10.1021/bi400819x | *Biochemistry* 2013, 52, 6424−6436

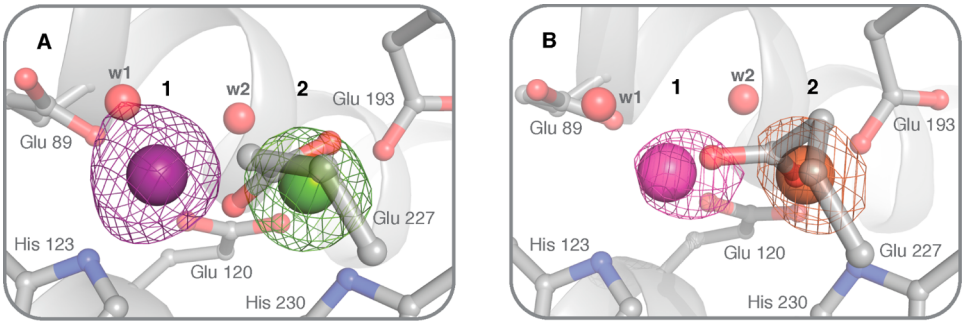

Figure 3. Metal site assignment from the anomalous X-ray scattering by Mn and Fe ions in crystals of *Ct* β_2. Selected active site residues are shown as sticks. Metal ions and water molecules are shown as spheres. Mn is at site 1 and Fe is at site 2. Anomalous difference density is not observed above background (5.0−6.0σ) in the opposite site for either metal. (A) From crystals of Mn^{II}/Fe^{II}-β_2 obtained by loading apo β_2 with 1 equiv of each metal per monomer followed by anaerobic crystallization, anomalous difference maps were obtained for both Mn (purple mesh) and Fe (green mesh) and are shown contoured at 6.0σ. (B) Samples of Mn^{IV}/Fe^{III}-β_2 for crystallization were prepared by procedure 3B [anaerobic loading of 1 equiv each of Mn^{II} and Fe^{II} per β monomer followed by O_2 exposure (see Table 2)]. From the resultant crystals, anomalous difference maps were obtained for Mn (pink mesh) and Fe (orange mesh) and are shown contoured at 5.0σ.

the apoprotein with 1 equiv each (per β monomer) of Mn^{II} and Fe^{II} (2 equiv total) and crystallizing the resulting metal-loaded protein anaerobically (Table S2 of the Supporting Information). Diffraction data were collected at the Mn and Fe X-ray absorption K-edges to calculate Mn- and Fe-specific anomalous difference maps, respectively (Figure 3A), and assign metal site occupancies. Because Mn contributes significantly to the X-ray absorption at the Fe K-edge, the Fe-specific difference map was generated by a subtraction procedure[39] to eliminate the contribution from Mn. These maps indicate that Mn^{II} binds at site 1 and Fe^{II} at site 2. Importantly, this result provides further evidence that the (more) active cofactor configuration contains Mn^{IV} at site 1 and Fe^{III} at site 2, as suggested by previous crystallographic characterization of the oxidized form.[21,22] However, in this new structure, the metal ions appear to have partitioned into their functional sites with greater selectivity. In all four views of the metal binding site, Mn anomalous density at site 2 is below the background level (5.0−6.0σ)[43] (Table 1), and no anomalous density for Fe is seen at site 1 (Table S9 of the Supporting Information).[44] The most obvious difference in the metal loading strategy employed here is the provision of both metals in a 1:1 stoichiometry per β monomer prior to any exposure to O_2. This procedure should, in contrast to those used in the previous studies, permit the Mn^{II} and Fe^{II} ions to reach equilibrium within the metal binding site over a period of days while crystallization occurs. In other words, metal binding should, in this case, be solely under thermodynamic control. Excitingly, this result suggests that the protein scaffold provides an intrinsic basis for localizing Mn^{II} to site 1 and Fe^{II} to site 2, even with the more labile divalent metal ions.

Our successful crystallization of *Ct* β_2 with bound Fe^{II} is somewhat surprising because, to date, no crystal structure of a class I β_2 protein has been determined with Fe^{II} introduced during crystallization. The difficulty in crystallizing $Fe_2^{II/II}$ forms of the protein is believed to result from the dynamic nature of the interaction between Fe^{II} and the β_2 metal binding sites. $Fe_2^{II/II}$-β_2 structures have instead been determined by soaking apoprotein crystals with Fe^{II} ions[25,27] or by chemical reduction or photoreduction of crystals of $Fe_2^{III/III}$-β_2.[28,29] The former approach, soaking metal ions into the apoprotein, has yielded structures differing from those obtained after reduction of $Fe_2^{III/III}$-β_2. The structures obtained by Fe^{II} soaks are more consistent with circular dichroism and magnetic circular dichroism characterization of the $Fe_2^{II/II}$ state[45] and thus provide a more appropriate starting point for analysis of the O_2 reaction. The cocrystallization approach used here for *Ct* Mn^{II}/Fe^{II}-β_2 should similarly afford the appropriate O_2 reactive state. It is possible that the presence of Fe^{II} in a heterobimetallic cluster with Mn^{II} or specific properties of the cofactor site in *Ct* β_2 promote more stable Fe^{II} binding. An alternative scenario is that, even though the protein was crystallized and prepared for X-ray data collection in a stringently anaerobic environment, the sample became oxidized by trace O_2 and subsequently crystallized as the oxidized form. Several observations provide an argument against this possibility. The long Mn−Fe separation of 3.2 Å (compared to the distance of 2.9 Å determined by extended X-ray absorption fine structure spectroscopy for the Mn^{IV}/Fe^{III} state) and the long 2.1−2.3 Å bonds between the Mn and Fe ions and the bridging water ligand (Figure 4) are more

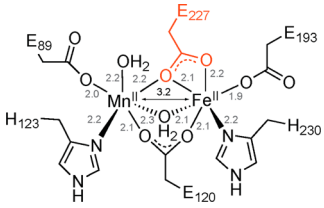

Figure 4. Schematic depiction of the cofactor site in Mn^{II}/Fe^{II}-β_2. Bond distances are given in angstroms. The μ-η^1,η^2 bridging ligand Glu 227 is colored red.

consistent with a lower oxidation state of the cluster (e.g., Mn^{II}/Fe^{II}). Although these structural features could potentially have arisen from photoreduction of oxidized Mn/Fe centers during data collection at 100 K,[46] the observed μ-η^1,η^2 binding mode of Glu 227 (Figures 1G and 4 and Figures S5 and S6 of the Supporting Information), also consistent with a reduced cofactor, is less likely to have arisen by cluster photoreduction and an accompanying carboxylate shift. We therefore conclude that the structure represents the Mn^{II}/Fe^{II} state and not a more oxidized form.

The resolution (1.8 Å) and homogeneous configuration of the Mn^{II}/Fe^{II} cofactor in this structure provide a basis for beginning to understand how the protein controls site selectivity during metal uptake and reaction with O_2 to form the active cofactor. The diffraction data were used to generate a fully refined model (Table S2 of the Supporting Information),

dx.doi.org/10.1021/bi400819x | *Biochemistry* 2013, 52, 6424−6436

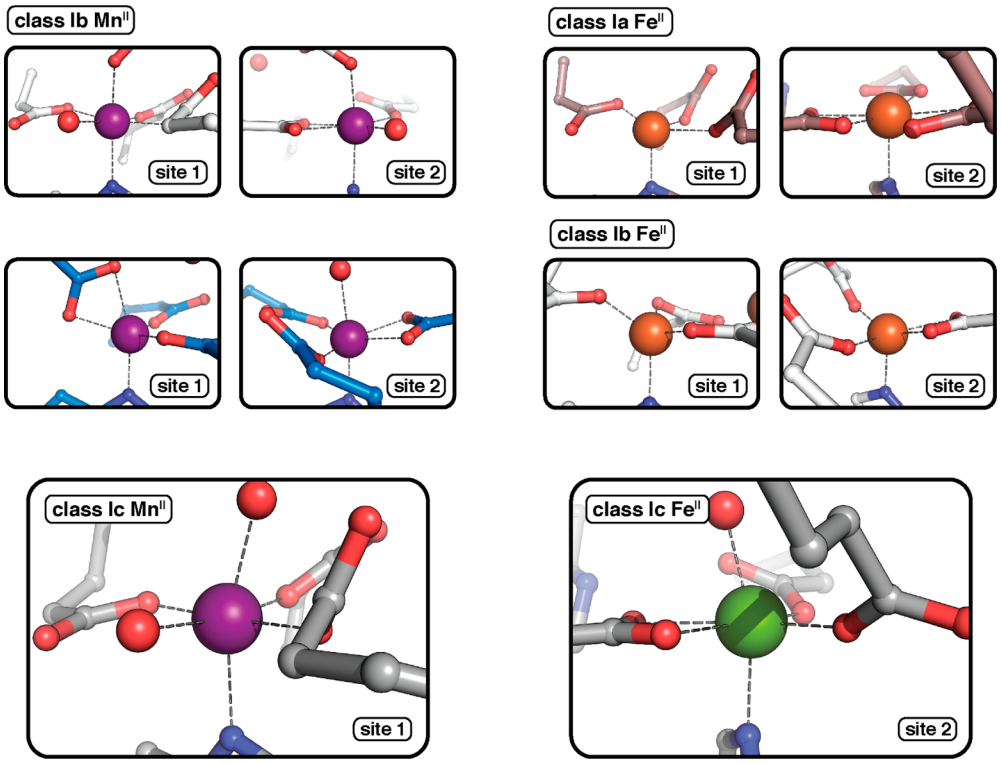

Figure 5. Representative Mn^{II} and Fe^{II} coordination geometries in class I RNRs. Class Ia $Fe_2^{II/II}$-β_2 (PDB entry 1PIY) and class Ib $Fe_2^{II/II}$-β_2 (PDB entry 3N38) structures were used to generate the Fe^{II} panels at the top left. Class Ib $Mn_2^{II/II}$-β_2 structures from the *Ec* (white, PDB entry 3N37) and *Bs* (blue, PDB entry 4DR0) enzymes were used to generate the Mn^{II} panels at the top right. Note that the Mn^{II} sites in the class Ib β_2 structures tend to exhibit higher coordination numbers with more strict adherence to octahedral geometry than the Fe^{II} coordination environments in the class Ia or Ib β_2 proteins. This trend is more apparent in the class Ib *Ec* $Mn_2^{II/II}$-β_2 structure than in the class Ib *Bs* $Mn_2^{II/II}$-β_2 structure, and interestingly, the *Ec* protein binds Mn^{II} more tightly than the *Bs* homolog.[9] Shown at the bottom is a comparison of the coordination environments in class Ic β_2 at site 1 (Mn^{II}, left) and site 2 (Fe^{II}, right). The binding sites in class Ic β_2 resemble those in the Mn^{II} structures from class Ib β_2 proteins in that they are six-coordinate with exogenous water ligands, but the geometric distortion, particularly axial to the His ligand, is similar to that of $Fe_2^{II/II}$-β_2 metal binding interactions.

in which the Mn^{II} and Fe^{II} ions at each metal binding site can be modeled at full or nearly full occupancy and the ligands are generally well-ordered (Figure S5 of the Supporting Information).[47] The first coordination sphere (Figure 1G) is similar to other structures of reduced class Ia and Ib β_2 proteins (Figure 1B,D,E).[25−27] Each metal ion is coordinated by a histidine and three carboxylate side chains, of which two (Glu 98 and Glu 227) bridge the metal ions. All metal−ligand bond distances fall within the range of 1.9−2.3 Å (Figure 4), similar to other Fe^{II}−O/N or Mn^{II}−O/N distances observed in class Ia and Ib β_2 crystal structures. The μ-η^1,η^2 coordination mode of Glu 227 found here is identical to that observed in other structures, obtained by soaking or cocrystallization methods, of reduced class I $Mn_2^{II/II}$- and $Fe_2^{II/II}$-β_2 proteins.[25,27] This chelating/bridging mode is distinct from the monodentate position adopted by the residue in structures of the corresponding oxidized complexes (Figure S6 of the Supporting Information).

Mn^{II}-occupied site 1 is six-coordinate with two exogenous solvent-derived molecules (modeled as waters w1 and w2) completing the first coordination sphere (Figures 1G and 4). High coordination numbers and the presence of bound water ligands have been observed in the structures of other Mn^{II}-substituted class Ia and Ib β_2 proteins (Figure 1D,E).[25,26,48] Interestingly, the class Ic Mn^{II}/Fe^{II}-β_2 structure shows significant distortion along the Mn^{II}−w2 axis (Figure 5), enforced by the position of Phe 197 in the outer sphere (Figure 1 and Figure S4 of the Supporting Information) and by the sharing of the w2 ligand with Fe^{II} at site 2 (Figures 1G and 5).

The configuration of Fe^{II} at site 2 is also distinct from those in the structures of Fe^{II}-substituted forms of other class I β_2 proteins. As for Mn^{II} at site 1, Fe^{II} is six-coordinate with a bound water ligand. In other class Ia and Ib β_2 structures, Fe^{II} exhibits highly distorted four- or five-coordinate geometries, and solvent waters are typically absent from the first coordination sphere (Figure 1B and Figure S6 of the Supporting Information).[25,27,45] The site 2 configuration in the Mn^{II}/Fe^{II} complex of *Ct* β_2 is also geometrically distorted along the Fe^{II}−w2 axis, for the same reasons cited above for site 1. More subtle distortion in the plane defined by the Glu ligands is also evident and arises from the mode of chelation of Glu 227 and the tightly constrained position of Glu 193, which results in a short (1.9 Å) Fe^{II}−O bond.

Comparison of the ligand positions in the apo and Mn^{II}/Fe^{II} forms of *Ct* β_2 (Figure 1F,G) reveals little change between the two, suggesting minimal net movement during metal uptake. The only significant ligand conformational change is a slight rotation of the Glu 120 carboxylate resulting in a *syn-syn* μ-1,3 bridging configuration. This coordination mode is also seen in the structures of class Ib β_2 proteins with Mn^{II} but differs from those in the Fe^{II}-substituted class Ia and Ib proteins, where it is either *syn-anti* or *anti-syn*.[25−27] The *syn-syn* mode may better accommodate the higher coordination numbers and octahedral

dx.doi.org/10.1021/bi400819x | *Biochemistry* 2013, 52, 6424−6436

geometry observed in other Mn^{II}_2-β_2 structures (Figure 5) and in the Mn^{II}/Fe^{II}-β_2 complex described here.

The Mn^{II}−Fe^{II} separation indicated by the crystallographic data is 3.2 Å. This value is unexpectedly short, especially when it is compared with the corresponding distances seen in other β_2 crystal structures in which Mn^{II}−Mn^{II} and Fe^{II}−Fe^{II} distances can range from 3.5 to 4.0 Å.[25−27,48] Indeed, even within the same protein scaffold (*Ct* β_2), the intermetal distance increases to 3.5 Å in the $Mn_2^{II/II}$ complex (*vide infra*), suggesting that only the fully occupied heterobimetallic state exhibits the close approximation of the metal ions in the reduced cluster form. Recent X-ray absorption spectroscopic characterization reported a Mn−Fe separation of 3.5−3.65 Å in forms of the enzyme generated by chemical reduction or following prolonged exposure to X-ray radiation (presumably generating primarily Mn^{II}/Fe^{II} clusters).[46] However, the lack of identification and quantification of all cluster forms present in those samples render interpretation of the results perilous. The 3.2 Å Mn−Fe distance observed here is comparable to the Fe^{II}−Fe^{II} distance (3.3 Å) found in a crystal structure of the reduced ($Fe_2^{II/II}$) form of soluble methane monooxygenase hydroxylase (sMMOH),[49] a distantly related member of the large family of ferritin-like dimetal-carboxylate proteins.[50,51] Interestingly, the two defining substitutions that distinguish the class Ic *Ct* β_2 protein from the class Ia and Ib orthologs (Glu 89 in place of Asp in metal site 1 and Phe 127 at the position corresponding to the radical tyrosine) are also preserved in sMMOH as a Glu and Cys, respectively. The comparison suggests that the larger carboxylate ligand at site 1 and outer sphere interactions may favor a closer approach of the divalent metals. In terms of function, the proximity of the metal centers in the Mn^{II}/Fe^{II} complex of *Ct* β_2 could have important implications for the mechanism of the activation reaction, especially the mode of initial addition of O_2 to the reduced cluster.

Crystallographic Analysis of Mn^{II}-β_2. X-ray diffraction data sets collected on crystals of *Ct* β_2 grown from the protein loaded with Mn^{II} only (Figure S7 and Tables S3 and S4 of the Supporting Information) reveal partial metal occupancy of both site 1 and site 2. The observed occupancies could result from binding of Mn^{II} to site 1 in 50% of the β monomers and to site 2 in the other 50%. Alternatively, it could also be the outcome of highly cooperative binding of Mn^{II} to form a fully occupied $Mn_2^{II/II}$ cluster in half of the monomers and an unoccupied apo site in the other half. We also attempted X-ray diffraction experiments on crystals exposed (during cocrystallization or in crystal soaking experiments) to Mn^{II} in excess of the number of binding sites in an effort to achieve a fully occupied $Mn_2^{II/II}$ center in both subunits. These efforts yielded, at maximum, 90% occupancy of site 2 and 70% occupancy of site 1 (metal ion occupancies determined by refinement[41] and visual inspection of the $F_o - F_c$ difference map). The metal−metal distance is 3.5 Å in these structures, and two waters are present at positions similar to those in the Mn^{II}/Fe^{II} structure except the Mn^{II}−OH_2 distances are much longer (2.3−2.4 Å). These structures highlight the difficulty in forming a fully occupied $Mn_2^{II/II}$ cluster in this protein and show that Mn^{II} does not localize solely to site 1 in the absence of Fe^{II}. Additionally, loading of Mn^{II} does not induce significant conformational changes in the metal binding site.

Reconstitution of Active Mn^{IV}/Fe^{III}-β_2 and Crystallographic Confirmation of Metal Site Selectivity. The Mn^{II}/Fe^{II}-β_2 complex implies that Mn^{II} binds only at site 1 and Fe^{II} only at site 2 when the divalent metal ions are provided in the proper proportions and allowed to reach equilibrium in the absence of O_2 (i.e., controlled by the binding thermodynamics rather than kinetics, as in previous studies). This finding suggested that reconstituting the protein in this manner might afford homogeneous and maximally active preparations. To test this prediction, we evaluated samples activated by three different procedures, each starting with a different Mn^{II}:Fe^{II} ratio (Table 2, procedures 3A−3C). In procedure 3A, Mn^{II} was added at a level of 2 equiv and Fe^{II} at a level of 0.65 equiv per β monomer. In procedure 3B, Mn^{II} and Fe^{II} were added in equal quantities, each at 1 equiv per β. In procedure 3C, Fe^{II} was added at a level of 2 equiv and Mn^{II} at a level of 0.65 equiv per β. In each case, the cofactor was assembled by allowing the divalent metal ions to bind and reach equilibrium prior to the addition of O_2. Following removal of unincorporated metal ions by dialysis of the protein against EDTA-supplemented buffer (excess EDTA was removed by further dialysis against buffer lacking EDTA), the resultant Mn^{IV}/Fe^{III}-β_2 complexes were analyzed by ICP-AES (metal quantification), X-ray crystallography, EPR spectroscopy, and RNR activity assays. Although the quantity of total metal added to β_2 was sufficient to support full occupancy, ICP-AES analysis revealed that the protein retained ∼50% of the total metal added (Table 2). This result is consistent with previous observations that the stoichiometry of functional metal sites is less than the theoretical complement.[21,52] The retained Mn:Fe ratio was roughly 1:1 in the procedure 3A and procedure 3B samples, whereas the procedure 3C sample, not surprisingly, retained significantly more Fe than Mn. The ability of these preparations of Mn^{IV}/Fe^{III}-β_2 to support ribonucleotide reduction was assessed using the published liquid chromatography−mass spectrometry assay.[14] The preparations were found to possess the greatest catalytic activity per β monomer (Table 2) yet reported.[21] On a per Mn basis, the activities are comparable to those of samples from the previous study that were shown by X-ray crystallography to contain Mn primarily at site 1.[21] After reduction of the Mn^{IV}/Fe^{III} complexes to the EPR active Mn^{III}/Fe^{III} state by treatment with dithionite, X-band EPR spectra were acquired (Figure S8 of the Supporting Information). The spectra are similar to those previously assigned to Mn^{III}/Fe^{III}-β_2 complexes with Mn^{III} almost exclusively at site 1 (procedure 2) and different from those arising from samples with a potentially more heterogeneous distribution of Mn^{III}/Fe^{III} and Fe^{III}/Mn^{III} clusters (procedure 1).[21] These results indicate that the new reconstitution procedure (relying on the thermodynamic control of Mn^{II} and Fe^{II} binding to the apoprotein) yields more selective incorporation of Mn at site 1, generating preparations with greater catalytic activity than previously reported.

Crystals were grown from the samples reconstituted to the active state by procedure 3A and procedure 3B. X-ray diffraction data were collected (Tables S5 and S6 of the Supporting Information) at wavelengths appropriate for calculation of Mn- and Fe-specific anomalous difference maps (Figure 3B) and location of the metals in the active site. In each case, the crystals contain four β monomers per ASU, offering four independent views of the metal binding site. In all eight views, the Mn anomalous scattering peaks dominate in site 1 (Table 1) and the peak heights in site 2 are well below the background level (defined as 5.0−6.0σ). The anomalous scattering data demonstrate that Mn partitions cleanly into site 1 and Fe into site 2 in these samples, as found in the structure of the Mn^{II}/Fe^{II}-β_2 complex.

dx.doi.org/10.1021/bi400819x | *Biochemistry* 2013, 52, 6424−6436

The structural features of the cofactor site are generally consistent with those found in the published structures of protein crystallized as the $Fe_2^{III/III}$ and Mn^{IV}/Fe^{III} complexes of *Ct* β_2.[21,42] The electron density maps suggest that Glu 227 moves from a μ-η^1,η^2 bridging position to a monodentate coordination mode at site 2 during the activation reaction (Figure S6 of the Supporting Information), consistent with analogous carboxylate shifts that have been proposed in other class I β_2 proteins.[52] In addition, two new (nonprotein) bridging oxygen ligands, which could presumably originate from O_2 as it is reduced to the oxidation state of water during the reaction, are evident in the oxidized complex. However, the modest resolution (1.90−2.20 Å) and low overall metal occupancy (<50%) limit our ability to elicit additional structural details for the oxidized cluster. The active metallocofactor is susceptible to X-ray-induced photoreduction,[20,46] as is generally a major challenge in accurate structural characterization of high-valent metalloenzyme intermediates by X-ray crystallography.[53] The effects of X-ray photoreduction during cryocrystallography, with the sample maintained at 100 K during data collection, are probably limited to slight elongation of metal−ligand bonds and metal−metal distances rather than large-scale ligand movements and dissociations. Thus, the conformational change of Glu 227 and introduction of new bridging oxygen ligands observed in the structure of the oxidized complex[21,42] (Figure S6 of the Supporting Information) are very likely to be authentic structural changes associated with activation. A complete picture of the structure of the active metallocofactor will require corroborating data from an ensemble of methods as well as a still-absent high-resolution X-ray crystal structure of *Ct* β_2 with a fully occupied and homogeneous Mn^{IV}/Fe^{III} cluster.

DISCUSSION

Structural Basis for Metal Ion Site Selectivity. A comparison of the coordination environment in the Mn^{II}/Fe^{II} complex of *Ct* β_2 to those in the homodinuclear ($Fe_2^{II/II}$ or $Mn_2^{II/II}$) complexes of the class Ia or Ib β_2 proteins provides a rationale for how the structure of the class Ic β_2 protein might direct Mn^{II} to site 1 and Fe^{II} to site 2. The most relevant comparisons for understanding the occupancy of site 1 by Mn^{II} are to the structures of the class Ib $Mn_2^{II/II}$-β_2 proteins,[25,26] enzymes in which the $Mn_2^{II/II}$ state is the relevant starting point for cofactor activation[8−10,54] and the cofactor site is therefore expected to be optimized for Mn^{II} selectivity. In these structures, the Mn^{II} centers are five- or six-coordinate and include exogenous solvent ligands in the primary coordination sphere (Figures 1 and 5). As observed previously,[25,26] the geometry trends toward an ideal octahedron, a configuration typical of a high-spin Mn^{II} d^5 electronic configuration.[55] High-affinity Mn^{II} binding sites in other proteins such as calprotectin[56,57] and Mn catalase[58] are also commonly six-coordinate with octahedral geometry. In the *Ct* Mn^{II}/Fe^{II}-β_2 structure, both metal sites are six-coordinate and have exogenous solvent ligands, but severe distortion exists at each site along the w2 axis, enforced by the position of a Phe residue between the two sites (Figure 1 and Figure S4 of the Supporting Information). The position and bulky nature of the Phe side chain make it impossible for the water to bind solely to the Mn^{II} ion at site 1 or for each metal to coordinate an axial water. The distortion at site 2 is perhaps made even more pronounced by the chelating mode of Glu 227 at site 2 and the short metal−ligand bond with Glu 193 (Figure 5). These binding modes are driven by a hydrogen bonding network in the secondary sphere (Figure S4 of the Supporting Information) that forces Glu 193 into a tight monodentate binding mode with the site 2 metal, opening a coordination position that is filled by the chelating interaction with Glu 227 at this site. The six-coordinate environment and the ability to accommodate waters in the first coordination sphere may favor occupancy by Mn^{II} at both sites, but it is not obvious that site 1 should be more stringent than site 2 in the selectivity for Mn^{II} over Fe^{II}. An alternative proposal is that the geometric distortion, particularly at site 2, could favor Fe^{II} binding by stabilizing the asymmetrically filled t_{2g} subshell of a high-spin d^6 electronic configuration in a weak octahedral ligand field.[55] Distortions of this type in Fe^{II} complexes have been predicted computationally,[59] and the observation that other class I β_2 structures with Fe^{II} exhibit lower coordination numbers and distorted geometries[25,27] lends further support to this mechanism for enforcing Fe^{II} selectivity at site 2.

The seemingly rigid nature of the metal binding sites in *Ct* β_2 and the influence of the surrounding protein in defining the coordination geometry are reminiscent of the entatic-state model for metal−protein interactions.[60] Here, the metal binding site of *Ct* β_2 could perhaps be viewed as an entatic state designed to select between two different metals with subtly different coordination preferences. The geometry of the *Ct* β_2 metal binding sites imposes a sufficiently unfavorable environment for Mn^{II} interaction that Fe^{II} is allowed to displace it, particularly at site 2. This strategy would lead to the selective formation of the Mn^{II}/Fe^{II} cluster when Mn^{II} is in excess and Fe^{II} is limiting. Additional experimental analysis will be necessary to validate this model for class Ic metallocofactor assembly. The rigid nature of much of the class Ic β_2 ligand framework after metal binding is also likely to be important in the O_2 reaction to activate the cofactor and in control of the reversible RT that initiates and terminates nucleotide reduction.

The observation from the class Ic β_2 structures that the ligands remain in largely the same position in the presence and absence of the metal ions stands in stark contrast to the situations in the class Ia and Ib proteins.[23,24] In comparison to their apoproteins, the metal-bound forms (Figure 1) in these systems show changes in the conformations and/or positions of several ligands, particularly the residues cognate to *Ct* β_2 Glu 193.[25−27] Conformational changes of side chains during metal binding in class Ia or Ib β_2 proteins could encourage cooperative binding to favor efficient assembly of the appropriate homodinuclear metallocofactor precursor. Conversely, the near complete absence of ligand movement upon metal binding to the class Ic β_2 could be part of an adaptation to inhibit formation of $Mn_2^{II/II}$ or $Fe_2^{II/II}$ centers that would ultimately lead to an inactive cofactor.

Structural Insight into Oxidative Activation of the Cofactor by O_2. The next step in metallocofactor assembly in *Ct* β_2 is the reaction of the Mn^{II}/Fe^{II} center with O_2 to form the Mn^{IV}/Fe^{IV} intermediate,[13] which, upon one-electron reduction of the Fe^{IV} site, is converted to the stable and active Mn^{IV}/Fe^{III} state.[12,17] The location and mode of O_2 addition and the protein structural changes that accompany the reaction are not known. O_2 is likely to interact first with Fe^{II}, which has the more appropriate oxidation potential for reducing O_2.[61] With firm evidence now in hand that Fe^{II} is located at site 2, the proposal that O_2 adds to Fe^{II} aligns with studies of the class Ia *Ec* β_2 oxygen binding site[62] and analysis of crystal structures of the reactant ($Mn_2^{II/II}$) forms of class Ib β_2,[25,26] which all suggested that the oxidant (O_2 or $O_2^{\bullet-}$) adds first to the site 2 metal.

dx.doi.org/10.1021/bi400819x | *Biochemistry* 2013, 52, 6424−6436

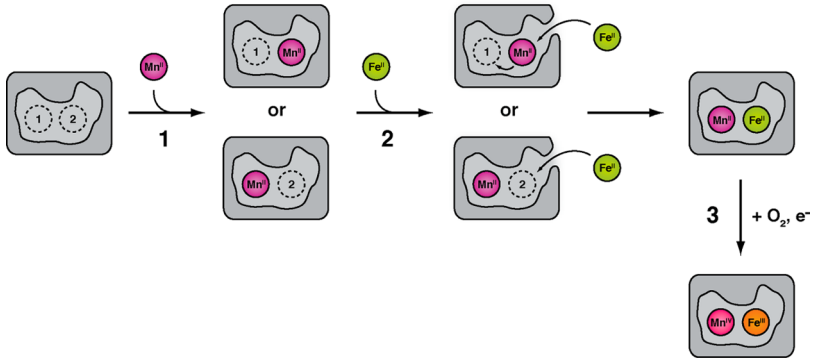

Figure 6. Model for *in vivo* cofactor assembly in the β_2 subunit of *Ct* class Ic RNR. In step 1, Mn^{II} ion is taken up by the apoprotein first with little to no preference for site 1 or site 2. In the second step, Fe^{II} ions bind selectively to site 2. The preference of site 2 for Fe^{II} could be controlled in part by the rigid, distorted six-coordinate geometry of the β_2 metal binding sites. *In vivo*, site specificity could be enhanced by the action of a chaperone delivering Fe^{II} to site 2 via a specific pathway. Reaction with the oxidant occurs in step 3. The model posits that the preference of Fe^{II} for site 2 drives formation of the Mn^{II}/Fe^{II} cluster instead of the Fe^{II}/Mn^{II} form to ensure efficient production of the more active Mn^{IV}/Fe^{III} state.

Comparison of the structure of the oxidized form of the class Ic β_2 to that of the reduced (Mn^{II}/Fe^{II}) form reveals additional clues about how O_2 might interact with the Fe^{II} center. The cofactor of the Mn^{II}/Fe^{II}-β_2 complex lacks open coordination sites, suggesting that O_2 must displace existing ligands. The most likely candidates to be displaced are the bridging H_2O (w2) and Oε atom of Glu 227. The latter shift would move the carboxylate toward its observed position in the oxidized complex. Similar shifts in the analogous Glu ligand are proposed in metallocofactor activation of certain class Ia and class Ib β_2 proteins.[8,25−27,30] Whereas the class Ia β_2 proteins are proposed to form peroxo-$Fe_2^{III/III}$ complexes after O_2 addition,[63,64] such a peroxo intermediate involving the Mn ion has not been observed during activation of *Ct* β_2. Addition of O_2 to the Fe site might instead yield a Mn^{II}/Fe^{III}-η^2-superoxo complex. Attack of the Mn^{II} on the O−O unit would cleave this bond and generate the observed Mn^{IV}/Fe^{IV} intermediate directly. Crucial for this alternative mechanism is the unusually close approximation of the reduced metal ions, 3.2 Å apart, which would appropriately position the Mn^{II} ion for attack. The proposed initial mixed-valent Mn^{II}/Fe^{III}-superoxo species may be analogous to a Mn^{II}/Mn^{III}-peroxo complex recently proposed as an intermediate in activation of class Ib $Mn_2^{II/II}$-β_2.[9]

Implications for Metallocofactor Biosynthesis *in Vivo*. The factors that control *in vivo* metalation of class I β_2 with Fe or Mn are not well understood. In fact, elucidation of the most active versions of the class Ib and Ic metallocofactors (including *Ct* β_2) has been hampered by the ease with which the β_2 scaffold can be mismetalated, especially during heterologous overexpression in *E. coli*.[65] Metalation in class Ia or Ib RNRs is most likely controlled by differential expression of proteins based on Mn^{II} or Fe^{II} availability (or perhaps metallochaperone intervention in some systems) rather than being dependent on the intrinsic metal ion affinities of a given β_2 scaffold and its metal binding sites.[65] In class Ic RNR, use of a mixed Mn/Fe metallocofactor requires that both metals must be somewhat bioavailable for the cofactor to assemble at all. Furthermore, if the Mn^{IV}/Fe^{III} configuration is the only active form (as opposed to the Fe^{III}/Mn^{IV} arrangement), then there must be some basis for directing Mn to site 1 and Fe to site 2. The X-ray structures reported here suggest that metal ion partitioning to the appropriate site can occur during the metal binding step. Because this happens *in vitro* without the aid of chaperones or other accessory factors, the protein itself possesses a remarkable intrinsic metal ion binding selectivity at each site. However, the requirement for relatively strict thermodynamic and stoichiometric control of metal binding to generate homogeneous active preparations suggests that the relative levels of Mn^{II} and Fe^{II} within the cell and their order of addition in conjunction with the oxidant could be quite important in assembly of the class Ic β_2 metallocofactor.

The basis for the intrinsic metal ion binding selectivity remains to be established, but we suggest that the unusually rigid positioning of the ligands in *Ct* β_2 in a distorted octahedral geometry, especially at site 2, could disfavor binding of Mn^{II} to site 2 and thereby favor binding of Fe^{II} there. In our working hypothesis for *in vivo* metallocofactor assembly (Figure 6), Mn^{II} interacts first with the β_2 metal binding site without preference for site 1 or site 2. Fe^{II} adds second, with a stronger affinity for site 2. This step could be facilitated by a metallochaperone or simply by limiting the available Fe^{II} within the cell to <1 equiv per β monomer. Only with Fe^{II} bound is the protein reactive to O_2, and activation to the exchange-inert Mn^{IV}/Fe^{III} state can then proceed. This model differs from previously proposed models, in which affinity of a specific site for Mn^{II} has been suggested to drive formation of the appropriately metalated state.[52,66] The use of the Mn/Fe cofactor by *Ct* β_2 was initially rationalized as a mechanism for resisting oxidative stress experienced during infection by obviating the $Tyr^{\bullet}$,[12,42] which is known to be sensitive to nitric oxide and superoxide in the $Fe_2^{III/III}$-$Tyr^{\bullet}$ metallocofactors of class Ia RNRs.[67,68] Our model for class Ic metallocofactor biosynthesis suggests that use of the Mn^{IV}/Fe^{III} cofactor could, in addition, be an adaptation to Fe^{II} limitation.

The structures presented suggest a basis for the assembly of the novel heterodinuclear Mn^{IV}/Fe^{III} cofactor of *Ct* RNR. The structure of the apoprotein reveals a metal binding site templated for selecting and activating a heterobimetallic Mn^{II}/Fe^{II} center with Mn^{II} at site 1 and Fe^{II} at site 2, but our *in vitro* reconstitution experiments show that this selectivity is achieved only if the divalent metals are allowed to reach their equilibrium configuration within the protein prior to exposure to O_2. The observation that the interatomic Mn^{II}−Fe^{II} distance in the reduced cofactor (3.2 Å) is much shorter than metal−metal distances seen in structures of homodinuclear $Mn_2^{II/II}$ and $Fe_2^{II/II}$ complexes of class Ia and Ib β_2s suggests that close approximation of the two metal ions could be an adaptation to

dx.doi.org/10.1021/bi400819x | *Biochemistry* 2013, 52, 6424−6436

promote efficient oxidation of the Mn^{II}/Fe^{II} cluster by O_2 despite the presence of the Mn^{II}, intrinsically less reducing than a second Fe^{II}. The homogeneous metallocofactor in the Mn^{II}/Fe^{II}-β_2 structure provides a credible starting point for computational evaluation of the O_2 reaction coordinate in the class Ic system. The relatively small number of conformational changes seen in the structures of apo, Mn^{II}/Fe^{II}, and oxidized β_2 in this system may make it especially amenable to computational analysis of metallocofactor assembly. The structures additionally provide clues about the *in vivo* assembly of a mixed-metal cofactor, suggesting that the class Ic β_2 scaffold provides a platform that can successfully assemble an active Mn^{IV}/Fe^{III} center under conditions in which Mn^{II} is relatively abundant and Fe^{II} is limited.

■ ASSOCIATED CONTENT

Supporting Information

Tables S1−S9 and additional figures. This material is available free of charge via the Internet at http://pubs.acs.org.

Accession Codes

The coordinates of *C. trachomatis* apo and Mn^{II}/Fe^{II}-β_2 have been deposited in the Protein Data Bank as entries 4M1H and 4M1I, respectively.

■ AUTHOR INFORMATION

Corresponding Author

*E-mail: akb20@psu.edu. Telephone: (814) 867-2863.

Present Addresses

[§]L.M.K.D.: Department of Molecular Biosciences, Northwestern University, Evanston, IL 60208.

[∥]A.K.B.: Department of Biochemistry and Molecular Biology and Department of Chemistry, The Pennsylvania State University, University Park, PA 16802.

Funding

This work was supported by National Institutes of Health (NIH) Grants GM58515 (A.C.R.) and GM55365 (J.M.B. and C.K.), an Alfred P. Sloan Foundation scholarship to L.M.K.D., and an NIH Pathway to Independence award to A.K.B.

Notes

The authors declare no competing financial interest.

■ ACKNOWLEDGMENTS

Use of the Advanced Photon Source, an Office of Science User Facility operated for the U.S. Department of Energy (DOE) Office of Science by Argonne National Laboratory, was supported by the U.S. DOE under Contract DE-AC02-06CH11357. Use of LS-CAT Sector 21 was supported by the Michigan Economic Development Corp. and the Michigan Technology Tri-Corridor (Grant 085P1000817). GM/CA-CAT has been funded in whole or in part with Federal funds from the National Cancer Institute (Y1-CO-1020) and the National Institute of General Medical Sciences (Y1-GM-1104). A.K.B. thanks Joey Cotruvo and Harry Gray for helpful discussions about Mn^{II} and Fe^{II} coordination chemistry.

■ ABBREVIATIONS

RNR, ribonucleotide reductase; *Ct*, *Chlamydia trachomatis*; β_2, ribonucleotide reductase small subunit containing the metallocofactor; RT, radical translocation; $Tyr^{\bullet}$, tyrosyl radical; *Ec*, *Escherichia coli*; *Bs*, *Bacillus subtilis*; SSM, secondary structure matching; ASU, asymmetric unit; ICP-AES, inductively coupled plasma atomic emission spectroscopy; PDB, Protein Data Bank.

■ REFERENCES

(1) Stubbe, J. (2000) Ribonucleotide reductases: The link between an RNA and a DNA world? *Curr. Opin. Struct. Biol. 10*, 731−736.

(2) Nordlund, P., and Reichard, P. (2006) Ribonucleotide reductases. *Annu. Rev. Biochem. 75*, 681−706.

(3) Stubbe, J., Nocera, D. G., Yee, C. S., and Chang, M. C. Y. (2003) Radical initiation in the class I ribonucleotide reductase: Long-range proton-coupled electron transfer? *Chem. Rev. 103*, 2167−2201.

(4) Stubbe, J., and Ackles, D. (1980) On the mechanism of ribonucleoside diphosphate reductase from *Escherichia coli*. Evidence for 3′-C−H bond cleavage. *J. Biol. Chem. 255*, 8027−8030.

(5) Mao, S. S., Yu, G. X., Chalfoun, D., and Stubbe, J. (1992) Characterization of C439SR1, a mutant of *Escherichia coli* ribonucleotide diphosphate reductase: Evidence that C439 is a residue essential for nucleotide reduction and C439SR1 is a protein possessing novel thioredoxin-like activity. *Biochemistry 31*, 9752−9759.

(6) Atkin, C. L., Thelander, L., Reichard, P., and Lang, G. (1973) Iron and free radical in ribonucleotide reductase. Exchange of iron and Mössbauer spectroscopy of the protein β2 subunit of the *Escherichia coli* enzyme. *J. Biol. Chem. 248*, 7464−7472.

(7) Nordlund, P., Sjöberg, B.-M., and Eklund, H. (1990) Three-dimensional structure of the free radical protein of ribonucleotide reductase. *Nature 345*, 593−598.

(8) Cox, N., Ogata, H., Stolle, P., Reijerse, E., Auling, G., and Lubitz, W. (2010) A tyrosyl-dimanganese coupled spin system is the native metalloradical cofactor of the R2F subunit of the ribonucleotide reductase of *Corynebacterium ammoniagenes*. *J. Am. Chem. Soc. 132*, 11197−11213.

(9) Cotruvo, J. A., Jr., Stich, T. A., Britt, R. D., and Stubbe, J. (2013) Mechanism of assembly of the dimanganese-tyrosyl radical cofactor of class Ib ribonucleotide reductase: Enzymatic generation of superoxide is required for tyrosine oxidation via a Mn(III)Mn(IV) intermediate. *J. Am. Chem. Soc. 135*, 4027−4039.

(10) Cotruvo, J. A., Jr., and Stubbe, J. (2010) An active dimanganese(III)-tyrosyl radical cofactor in *Escherichia coli* class Ib ribonucleotide reductase. *Biochemistry 49*, 1297−1309.

(11) Bollinger, J. M., Jr., Edmondson, D. E., Huynh, B. H., Filley, J., Norton, J. R., and Stubbe, J. (1991) Mechanism of assembly of the tyrosyl radical-dinuclear iron cluster cofactor of ribonucleotide reductase. *Science 253*, 292−298.

(12) Jiang, W., Yun, D., Saleh, L., Barr, E. W., Xing, G., Hoffart, L. M., Maslak, M. A., Krebs, C., and Bollinger, J. M., Jr. (2007) A manganese(IV)/iron(III) cofactor in *Chlamydia trachomatis* ribonucleotide reductase. *Science 316*, 1188−1191.

(13) Jiang, W., Hoffart, L. M., Krebs, C., and Bollinger, J. M., Jr. (2007) A manganese(IV)/iron(IV) intermediate in assembly of the manganese(IV)/iron(III) cofactor of *Chlamydia trachomatis* ribonucleotide reductase. *Biochemistry 46*, 8709−8716.

(14) Jiang, W., Saleh, L., Barr, E. W., Xie, J., Gardner, M. M., Krebs, C., and Bollinger, J. M., Jr. (2008) Branched activation- and catalysis-specific pathways for electron relay to the manganese/iron cofactor in ribonucleotide reductase from *Chlamydia trachomatis*. *Biochemistry 47*, 8477−8484.

(15) Bollinger, J. M., Jr., Jiang, W., Green, M. T., and Krebs, C. (2008) The manganese(IV)/iron(III) cofactor of *Chlamydia trachomatis* ribonucleotide reductase: Structure, assembly, radical initiation, and evolution. *Curr. Opin. Struct. Biol. 18*, 650−657.

(16) Högbom, M. (2010) The manganese/iron-carboxylate proteins: What is what, where are they, and what can the sequences tell us? *JBIC, J. Biol. Inorg. Chem. 15*, 339−349.

(17) Jiang, W., Bollinger, J. M., Jr., and Krebs, C. (2007) The active form of *Chlamydia trachomatis* ribonucleotide reductase R2 protein contains a heterodinuclear Mn(IV)/Fe(III) cluster with S = 1 ground state. *J. Am. Chem. Soc. 129*, 7504−7505.

(18) Jiang, W., Xie, J., Nørgaard, H., Bollinger, J. M., Jr., and Krebs, C. (2008) Rapid and quantitative activation of *Chlamydia trachomatis* ribonucleotide reductase by hydrogen peroxide. *Biochemistry 47*, 4477−4483.

(19) Jiang, W., Xie, J., Varano, P. T., Krebs, C., and Bollinger, J. M., Jr. (2010) Two distinct mechanisms of inactivation of the class Ic ribonucleotide reductase from *Chlamydia trachomatis* by hydroxyurea: Implications for the protein gating of intersubunit electron transfer. *Biochemistry 49*, 5340−5349.
(20) Younker, J. M., Krest, C. M., Jiang, W., Krebs, C., Bollinger, J. M., Jr., and Green, M. T. (2008) Structural analysis of the Mn(IV)/Fe(III) cofactor of *Chlamydia trachomatis* ribonucleotide reductase by extended X-ray absorption fine structure spectroscopy and density functional theory calculations. *J. Am. Chem. Soc. 130*, 15022−15027.
(21) Dassama, L. M. K., Boal, A. K., Krebs, C., Rosenzweig, A. C., and Bollinger, J. M., Jr. (2012) Evidence that the β subunit of *Chlamydia trachomatis* ribonucleotide reductase is active with the manganese ion of its manganese(IV)/iron(III) cofactor in site 1. *J. Am. Chem. Soc. 134*, 2520−2523.
(22) Andersson, C. S., Öhrström, M., Popović-Bijelić, A., Gräslund, A., Stenmark, P., and Högbom, M. (2012) The manganese ion of the heterodinuclear Mn/Fe cofactor in *Chlamydia trachomatis* ribonucleotide reductase R2c is located at metal position 1. *J. Am. Chem. Soc. 134*, 123−125.
(23) Åberg, A., Nordlund, P., and Eklund, H. (1993) Unusual clustering of carboxyl side chains in the core of iron-free ribonucleotide reductase. *Nature 361*, 276−278.
(24) Högbom, M., Huque, Y., Sjöberg, B.-M., and Nordlund, P. (2002) Crystal structure of the di-iron/radical protein of ribonucleotide reductase from *Corynebacterium ammoniagenes*. *Biochemistry 41*, 1381−1389.
(25) Boal, A. K., Cotruvo, J. A., Jr., Stubbe, J., and Rosenzweig, A. C. (2010) Structural basis for activation of class Ib ribonucleotide reductase. *Science 329*, 1526−1530.
(26) Boal, A. K., Cotruvo, J. A., Jr., Stubbe, J., and Rosenzweig, A. C. (2012) The dimanganese(II) site of *Bacillus subtilis* class Ib ribonucleotide reductase. *Biochemistry 51*, 3861−3871.
(27) Voegtli, W. C., Sommerhalter, M., Saleh, L., Baldwin, J., Bollinger, J. M., Jr., and Rosenzweig, A. C. (2003) Variable coordination geometries at the diiron(II) active site of ribonucleotide reductase R2. *J. Am. Chem. Soc. 125*, 15822−15830.
(28) Eriksson, M., Jordan, A., and Eklund, H. (1998) Structure of *Salmonella typhimurium* NrdF ribonucleotide reductase in its oxidized and reduced forms. *Biochemistry 37*, 13359−13369.
(29) Logan, D. T., Su, X. D., Åberg, A., Regnström, K., Hajdu, J., Eklund, H., and Nordlund, P. (1996) Crystal structure of reduced protein R2 of ribonucleotide reductase: The structural basis for oxygen activation at a dinuclear iron site. *Structure 4*, 1053−1064.
(30) Nordlund, P., and Eklund, H. (1993) Structure and function of the *Escherichia coli* ribonucleotide reductase protein R2. *J. Mol. Biol. 232*, 123−164.
(31) The class Ib and Ic β_2 proteins can form O_2-reactive $Fe_2^{II/II}$ clusters *in vitro* or when overexpressed in a heterologous host. However, these clusters are either inactive (class Ic *Ct* RNR) or less active and apparently not utilized *in vivo* (all class Ib RNRs isolated from their native organisms to date).
(32) Otwinowski, Z., and Minor, W. (1997) Processing of X-ray diffraction data collected in oscillation mode. *Methods Enzymol. 276*, 307−326.
(33) McCoy, A. J., Grosse-Kunstleve, R. W., Storoni, L. C., and Read, R. J. (2005) Likelihood-enhanced fast translation functions. *Acta Crystallogr. D61*, 458−464.
(34) Murshudov, G. N., Vagin, A. A., and Dodson, E. J. (1997) Refinement of macromolecular structures by the maximum-likelihood method. *Acta Crystallogr. D53*, 240−255.
(35) Emsley, P., and Cowtan, K. (2004) Coot: Model-building tools for molecular graphics. *Acta Crystallogr. D60*, 2126−2132.
(36) *The PyMOL Molecular Graphics System* (2010) Schrödinger, LLC.
(37) Krissinel, E., and Henrick, K. (2004) Secondary-structure matching (SSM), a new tool for fast protein structure alignment in three dimensions. *Acta Crystallogr. D60*, 2256−2268.
(38) Ten Eyck, L. F. (1985) Fast Fourier transform calculation of electron density maps. *Methods Enzymol. 115*, 324−337.
(39) Than, M. E., Henrich, S., Bourenkov, G. P., Bartunik, H. D., Huber, R., and Bode, W. (2005) The endoproteinase furin contains two essential Ca^{2+} ions stabilizing its N-terminus and the unique S1 specificity pocket. *Acta Crystallogr. D61*, 505−512.
(40) Chen, V. B., Arendall, W. B., III, Headd, J. J., Keedy, D. A., Immormino, R. M., Kapral, G. J., Murray, L. W., Richardson, J. S., and Richardson, D. C. (2010) MolProbity: All-atom structure validation for macromolecular crystallography. *Acta Crystallogr. D66*, 12−21.
(41) Zwart, P. H., Afonine, P. V., Grosse-Kunstleve, R. W., Hung, L. W., Ioerger, T. R., McCoy, A. J., McKee, E., Moriarty, N. W., Read, R. J., Sacchettini, J. C., Sauter, N. K., Storoni, L. C., Terwilliger, T. C., and Adams, P. D. (2008) Automated structure solution with the PHENIX suite. *Methods Mol. Biol. 426*, 419−435.
(42) Högbom, M., Stenmark, P., Voevodskaya, N., McClarty, G., Gräslund, A., and Nordlund, P. (2004) The radical site in chlamydial ribonucleotide reductase defines a new R2 subclass. *Science 305*, 245−248.
(43) Vonrhein, C., Blanc, E., Roversi, P., and Bricogne, G. (2007) Automated structure solution with autoSHARP. *Methods Mol. Biol. 364*, 215−230.
(44) The procedure utilized for generating Fe-specific anomalous maps is not quantitative and underestimates the quantity of Fe present at a given site because it fails to account for the decay in Mn absorption with decreasing wavelength away from the Mn edge. Therefore, we report quantification of only the Mn anomalous signal in Table 1. Estimates for Fe occupancies are reported in Table S9 of the Supporting Information.
(45) Yang, Y. S., Baldwin, J., Ley, B. A., Bollinger, J. M., Jr., and Solomon, E. I. (2000) Spectroscopic and electronic structure description of the reduced binuclear non-heme iron active site in ribonucleotide reductase from *E. coli*: Comparison to reduced Δ^9 desaturase and electronic structure contributions to differences in O_2 reactivity. *J. Am. Chem. Soc. 122*, 8495−8510.
(46) Sigfridsson, K. G., Chernev, P., Leidel, N., Popović-Bijelić, A., Gräslund, A., and Haumann, M. (2013) Rapid X-ray photoreduction of dimetal-oxygen cofactors in ribonucleotide reductase. *J. Biol. Chem. 288*, 9648−9661.
(47) The data for Mn^{II} in site 1 are modeled best with 85−95% metal ion occupancy and the data for Fe^{II} at site 2 with 100% occupancy. The slightly diminished occupancy of Mn^{II} at site 1 may be significant, possibly reflecting a difference in affinities.
(48) Atta, M., Nordlund, P., Åberg, A., Eklund, H., and Fontecave, M. (1992) Substitution of manganese for iron in ribonucleotide reductase from *Escherichia coli*. *J. Biol. Chem. 267*, 20682−20688.
(49) Whittington, D. A., and Lippard, S. J. (2001) Crystal structures of the soluble methane monooxygenase hydroxylase from *Methylococcus capsulatus* (Bath) demonstrating geometrical variability at the dinuclear iron active site. *J. Am. Chem. Soc. 123*, 827−838.
(50) Sazinsky, M. H., and Lippard, S. J. (2006) Correlating structure with function in bacterial multicomponent monooxygenases and related diiron proteins. *Acc. Chem. Res. 39*, 558−566.
(51) Krebs, C., Bollinger, J. M., Jr., and Booker, S. J. (2011) Cyanobacterial alkane biosynthesis further expands the catalytic repertoire of the ferritin-like 'di-iron-carboxylate' proteins. *Curr. Opin. Chem. Biol. 15*, 291−303.
(52) Cotruvo, J. A., Jr., and Stubbe, J. (2011) Class I ribonucleotide reductases: Metallocofactor assembly and repair *in vitro* and *in vivo*. *Annu. Rev. Biochem. 80*, 733−767.
(53) Meharenna, Y. T., Doukov, T., Li, H., Soltis, S. M., and Poulos, T. L. (2010) Crystallographic and single-crystal spectral analysis of the peroxidase ferryl intermediate. *Biochemistry 49*, 2984−2986.
(54) Zhang, Y., and Stubbe, J. (2011) *Bacillus subtilis* class Ib ribonucleotide reductase is a dimanganese(III)-tyrosyl radical enzyme. *Biochemistry 50*, 5615−5623.
(55) Orgel, L. E. (1966) *An introduction to transition-metal chemistry: Ligand-field theory*, 2nd ed., pp 59−64, Wiley, New York.

(56) Hayden, J. A., Brophy, M. B., Cunden, L. S., and Nolan, E. M. (2013) High-affinity manganese coordination by human calprotectin is calcium-dependent and requires the histidine-rich site formed at the dimer interface. *J. Am. Chem. Soc. 135*, 775−787.
(57) Damo, S. M., Kehl-Fie, T. E., Sugitani, N., Holt, M. E., Rathi, S., Murphy, W. J., Zhang, Y., Betz, C., Hench, L., Fritz, G., Skaar, E. P., and Chazin, W. J. (2013) Molecular basis for manganese sequestration by calprotectin and roles in the innate immune response to invading bacterial pathogens. *Proc. Natl. Acad. Sci. U.S.A. 110*, 3841−3846.
(58) Antonyuk, S. V., Melik-Adamyan, V. R., Popov, A. N., Lamzin, V. S., Hempstead, P. D., Harrison, P. M., Artymyuk, P. J., and Barynin, V. V. (2000) Three-dimensional structure of the enzyme dimanganese catalase from *Thermus thermophilus* at 1 Å resolution. *Crystallogr. Rep. 45*, 105−116.
(59) Li, J., Fisher, C. L., Chen, J. L., Bashford, D., and Noodleman, L. (1996) Calculation of redox potentials and pK_a values of hydrated transition metal cations by a combined density functional and continuum dielectric theory. *Inorg. Chem. 35*, 4694−4702.
(60) Williams, R. J. P. (1995) Energised (entatic) states of groups and of secondary structures in proteins and metalloproteins. *Eur. J. Biochem. 234*, 363−381.
(61) Strumm, G., and Morgan, J. J. (1996) *Aquatic Chemistry*, pp 445, 672−690, Wiley, New York.
(62) Andersson, M. E., Högbom, M., Rinaldo-Matthis, A., Andersson, K. K., Sjöberg, B.-M., and Nordlund, P. (1999) The crystal structure of an azide complex of the diferrous R2 subunit of ribonucleotide reductase displays a novel carboxylate shift with important mechanistic implications for diiron-catalyzed oxygen activation. *J. Am. Chem. Soc. 121*, 2346−2352.
(63) Tong, W. H., Chen, S., Lloyd, S. G., Edmondson, D. E., Huynh, B. H., and Stubbe, J. (1996) Mechanism of assembly of the diferric cluster-tyrosyl radical cofactor of *Escherichia coli* ribonucleotide reductase from the diferrous form of the R2 subunit. *J. Am. Chem. Soc. 118*, 2107−2108.
(64) Yun, D., García-Serres, R., Chicalese, B. M., An, Y. H., Huynh, B. H., and Bollinger, J. M., Jr. (2007) (μ-1,2-Peroxo)diiron(III/III) complex as a precursor to the diiron(III/IV) intermediate X in the assembly of the iron-radical cofactor of ribonucleotide reductase from mouse. *Biochemistry 46*, 1925−1932.
(65) Cotruvo, J. A., Jr., and Stubbe, J. (2012) Metallation and mismetallation of iron and manganese proteins *in vitro* and *in vivo:* The class I ribonucleotide reductases as a case study. *Metallomics 4*, 1020−1036.
(66) Han, W. G., Giammona, D. A., Bashford, D., and Noodleman, L. (2010) Density functional theory analysis of structure, energetics, and spectroscopy for the Mn-Fe active site of *Chlamydia trachomatis* ribonucleotide reductase in four oxidation states. *Inorg. Chem. 49*, 7266−7281.
(67) Roy, B., Lepoivre, M., Henry, Y., and Fontecave, M. (1995) Inhibition of ribonucleotide reductase by nitric oxide derived from thionitrites: Reversible modifications of both subunits. *Biochemistry 34*, 5411−5418.
(68) Gaudu, P., Nivière, V., Petillot, Y., Kauppi, B., and Fontecave, M. (1996) The irreversible inactivation of ribonucleotide reductase from *Escherichia coli* by superoxide radicals. *FEBS Lett. 387*, 137−140.